Int. J. Heat Mass Transfer. Vol. 36, No. 2, pp. 249–263, 1993
Printed in Great Britain

0017-9310/93 $6.00+0.00
Pergamon Press Ltd

Natural convection liquid immersion cooling of a heat source flush mounted on a conducting substrate in a square enclosure

YOGENDRA JOSHI and L. O. HAUKENES
Naval Postgraduate School, Monterey, CA 93943, U.S.A.

and

SANJEEV B. SATHE
I.B.M. Corporation, Endicott, NY 13760, U.S.A.

(*Received* 4 *September* 1991 *and in final form* 9 *April* 1992)

Abstract—A numerical investigation of natural convection flow and heat transfer due to a rectangular heat source flush mounted on a substrate in a liquid-filled square enclosure was conducted. A finite volume model that accounts for the coupled conduction within the substrate and heat source and the natural convection in the liquid was utilized for a wide range of Rayleigh and Prandtl numbers. Little reduction in maximum temperatures was observed when substrate to fluid and component to fluid thermal conductivity ratios were increased beyond 10 and 25, respectively. Computed temperatures using the present model compared favorably with an existing experimental study.

INTRODUCTION

HEAT REMOVAL from electronic equipment is currently an area of extensive research and is likely to become even more important in the future due to the ever increasing component volumetric generation rates. Liquid immersion cooling has recently gained wide attention due to the need for increased power dissipation, the availability of inert dielectric liquids, and the introduction of immersion cooled supercomputers. Bar-Cohen [1] and Bergles and Bar-Cohen [2] have reviewed the research on single phase as well as phase change liquid cooling of electronic equipment. Incropera [3] provides a review of convective cooling of electronic components using air, as well as liquids.

Natural convection cooling has the advantages of simplicity of design and low operating costs due to no outside power requirements, minimum maintenance, absence of noise and high reliability. A number of studies [4–8] have examined natural convection from discrete heat sources in air. Natural convection in liquids results in significantly lower operating temperatures compared to those in air for the same input power and hence several experimental studies have recently been performed on transport from discrete heat sources in liquids. Park and Bergles [9] examined heat transfer from discrete sources on a vertical surface in extensive water and R-113 surroundings. Characteristics of discrete energy sources in liquid filled enclosures [10–12] and vertical channels [13] have also been examined experimentally.

Lee *et al.* [14] computed the two-dimensional natural convection from a heated protrusion in water. Three-dimensional computations of laminar natural convection in a rectangular liquid-filled enclosure containing a three by three array of heated protrusions were reported by Liu *et al.* [15]. In both studies uniform heat flux conditions were prescribed at the protrusion faces. Sathe and Joshi [16] conducted a two-dimensional numerical investigation of natural convection flow and heat transfer arising from a substrate mounted protruding heat source. Conduction heat transfer within the protrusion and substrate and the coupled natural convection in the liquid were computed without prescribing simplistic surface boundary conditions on the protrusion faces. Pronounced thermal spreading along the substrate was found for the low thermal conductivity electronic cooling liquids.

In the following, a computational study of laminar natural convection in a liquid-filled square enclosure from a discrete energy source flush mounted on a conducting vertical substrate is presented. A total of ten non-dimensional parameters govern the resulting transport. Out of these, five important ones were varied over wide ranges and their effects on transport studied. The computations show the strong influence of substrate conduction for dielectric liquids currently used in electronic cooling applications. The present model was also used to simulate a recent experimental

NOMENCLATURE

c_p	specific heat at constant pressure [J kg^{-1} K^{-1}]
d	dimension in Fig. 1 [m]
d_t	substrate thickness [m]
g	gravitational acceleration [m s^{-2}]
h	component height [m]
H	enclosure height [m]
k	thermal conductivity [W m^{-1} K^{-1}]
L_t	dimension in Fig. 1 [m]
p	pressure [N m^{-2}]
P	non-dimensional pressure, $p/\rho U_0^2$
Pr	Prandtl number, $\mu c_p/k_f$
q	non-dimensional heat flux (equation (7a))
Q	heat generation rate per unit length [W m^{-1}]
R_c	heat source to fluid thermal conductivity ratio, k_c/k_f
R_s	substrate to fluid thermal conductivity ratio, K_s/k_f
Ra	Rayleigh number, $g\beta Qh^3/\alpha k_f \nu$
$S1$	non-dimensional counter clockwise contour distance along the component-fluid/component-substrate interface
$S2$	non-dimensional counter clockwise contour distance along the solid–fluid interface
S_b, S_t	dimensions in Fig. 1 [m]
t_c	enclosure wall temperature [K]
T	non-dimensional temperature, $(t-t_c)/(Q/k_f)$
u	vertical velocity component [m s^{-1}]
U	non-dimensional vertical velocity component, u/U_0
U_0	reference velocity, $(g\beta Qh/k_f)^{1/2}$ [m s^{-1}]
v	horizontal velocity component [m s^{-1}]
V	non-dimensional horizontal velocity component, v/U_0
w	component width [m]
x	vertical coordinate [m]
X	non-dimensional vertical coordinate, x/h
y	horizontal coordinate [m]
Y	non-dimensional horizontal coordinate, y/h.

Greek symbols

α	fluid thermal diffusivity [m^2 s^{-1}]
β	coefficient of thermal expansion [K^{-1}]
δX	non-dimensional vertical distance between grid point and the control volume face
δY	non-dimensional horizontal distance between grid point and the control volume face
ρ	fluid density [kg m^{-3}]
μ	dynamic viscosity [kg m^{-1} s^{-1}]
ν	kinematic viscosity [m^2 s^{-1}]
κ_s	conductivity parameter for substrate $[R_s/(Ra\ Pr)^{1/2}]$
κ_c	conductivity parameter for heat source $[R_c/(Ra\ Pr)^{1/2}]$.

Subscripts

c	component (chip)
f	fluid/liquid
max	maximum
s	substrate
sur	substrate or component surface.

study in water and comparisons are presented between the numerically computed and measured heat source temperatures.

NUMERICAL MODEL

The schematic diagram of the configuration examined is shown in Fig. 1. A flush heat source mounted on a vertical substrate is immersed in a fluid-filled square enclosure of height H. Uniform volumetric heat generation takes place within the heater. The enclosure boundaries are maintained at a constant temperature, t_c. The heater, the substrate and the fluid have constant but different thermophysical properties. Assuming steady-state, negligible contract resistance between the heat source and substrate, laminar flow with no viscous dissipation and the Boussinesq approximations to be true, the dimensionless governing equations can be written as:

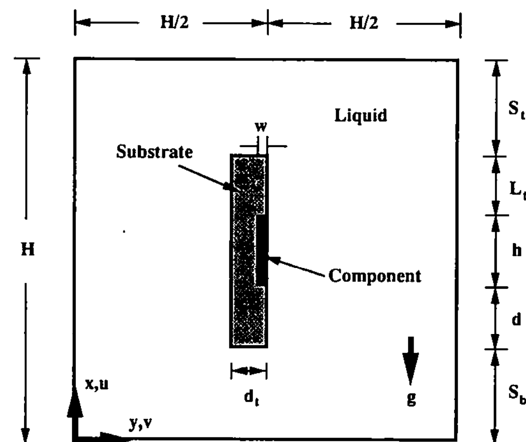

FIG. 1. Schematic diagram of configuration for numerical study.

Fluid region

$$\frac{\partial U}{\partial X}+\frac{\partial V}{\partial Y}=0 \quad (1)$$

$$\frac{\partial(U^2)}{\partial X}+\frac{\partial(UV)}{\partial Y} = (Pr/Ra)^{1/2}\left(\frac{\partial^2 U}{\partial X^2}+\frac{\partial^2 U}{\partial Y^2}\right)+T-\frac{\partial P}{\partial X} \quad (2)$$

$$\frac{\partial(UV)}{\partial X}+\frac{\partial(V^2)}{\partial Y} = (Pr/Ra)^{1/2}\left(\frac{\partial^2 V}{\partial X^2}+\frac{\partial^2 V}{\partial Y^2}\right)-\frac{\partial P}{\partial Y} \quad (3)$$

$$\frac{\partial(UT)}{\partial X}+\frac{\partial(VT)}{\partial Y} = (1/Ra\,Pr)^{1/2}\left(\frac{\partial^2 T}{\partial X^2}+\frac{\partial^2 T}{\partial Y^2}\right) \quad (4)$$

Solid region (heater)

$$\frac{\partial^2 T}{\partial X^2}+\frac{\partial^2 T}{\partial Y^2}=\frac{h}{wR_c} \quad (5)$$

Solid region (substrate)

$$\frac{\partial^2 T}{\partial X^2}+\frac{\partial^2 T}{\partial Y^2}=0 \quad (6)$$

where $X = x/h$, $Y = y/h$, $U = u/U_0$, $V = v/U_0$, $T = (t-t_c)/(Q/k_f)$, $P = p/\rho U_0^2$, $U_0 = (g\beta Qh/k_f)^{1/2}$, $Pr = \mu c_p/k_f$, $Ra = g\beta Qh^3/\alpha k_f \nu$, $R_c = k_c/k_f$ and $R_s = k_s/k_f$.

The enclosure walls are prescribed to be isothermal at temperature t_c and the no-slip and impermeable conditions for the velocity components are assumed, resulting in $U = V = T = 0$ at the enclosure walls. Heat fluxes are appropriately matched at the interfaces of dissimilar materials. The following governing parameters emerge as a result of the non-dimensionalized governing equations, boundary and matching conditions: Ra, Pr, R_c, R_s, S_b/h, d/h, L_t/h, S_t/h, w/h and w/d_t. The definitions of the symbols can be found in the Nomenclature.

The governing equations written in the primitive variables are discretized using a finite difference scheme wherein the control volumes for the temperature and pressure are staggered from those for the velocities. Power law profiles are used for the spatial variation of the dependent variables to ensure realistic results for a wide range of the grid Peclet numbers. Interface diffusivities are calculated using a harmonic-mean formulation in order to handle abrupt changes in the material properties. The details of the discretization process can be found in Patankar [17].

The discretized equations were solved iteratively using the line-by-line TDMA (tri-diagonal matrix algorithm) and the SIMPLER procedure as outlined by Patankar [17]. It is noted that even though separate equations are written for the fluid and solid regions, the latter is numerically simulated by prescribing a very large viscosity. Thus the same momentum equation is solved throughout the computational domain. Similarly, for the energy equation, heat sources and property values are used implicitly in the control volume formulation wherein mass, momentum and energy balances are incorporated for individual control volumes [17].

Test computations were performed on a series of non-uniform grids ranging from 30×30 to 73×73 control volumes to determine the grid size effects. More grid points were placed near the surfaces to capture adequately the large gradients. The values and locations for the maximum temperature and peak velocities did not change appreciably when the grid was refined beyond 40×40 control volumes. Most calculations were therefore performed on a grid size of 50×50. However for $Ra = 10^6$, the highest Ra in the present study, the solution did not converge on a 50×50 grid and it was found that by increasing the number of control volumes in the area of the suspected high thermal gradients, convergence could be achieved. Therefore, for $Ra = 10^6$ the number of control volumes was increased to 70×70. Convergence was based on a balance of the rate of energy generated in the component and the rate of energy leaving the enclosure walls. This balance was always better than 1%. At higher Ra, previously computed solutions at lower Ra were used as an initial guess in order to reduce run times.

The computational program was validated against two known natural convection flows. Natural convection in an enclosure with vertical hot and cold walls and adiabatic horizontal surfaces was computed to compare the present results with those of Raithby and Wong [18]. For an enclosure of aspect ratio 5 and Rayleigh numbers of 10^4 and 10^5 the agreement in the overall Nusselt numbers was better than 0.8%. The similarity solution for a line energy source at the leading edge of a vertical surface was also simulated by reducing the heat source size to a single control volume, setting $R_s \ll 1$ and moving the enclosure walls far away. Good agreement in the surface temperature response downstream of the source was found, as reported in ref. [16].

PARAMETRIC STUDY

Computations were made for various Ra, Pr, R_s and R_c values that would be found in actual cooling applications. Ra range from 10^3 to 10^6 was investigated with the upper limit due to the very slow convergence of the computations for larger Ra. The values of Pr, R_s and R_c were varied from 7 to 100, 0.1 to 100 and 1 to 100, respectively. The geometric parameters used in the computations were $S_b/h = 2$, $d/h = 2$, $L_t/h = 2$, $S_t/h = 3$, $w/h = 0.5$ and $w/d_t = 0.5$. A baseline study with $Ra = 10^5$, $Pr = 25$, $R_s = 10$ and $w/d_t = 0.5$ was conducted. The thermo-physical properties used in these parametric values correspond to the use of dielectric liquid FC 75 [19] as the coolant, epoxy-fiberglass as the substrate and a heat source

encapsulated within a ceramic package. When a particular parameter was being varied, all others were kept fixed at their baseline values.

A. *Effect of Ra*

The temperature contours for $Ra = 10^3$ to 10^6 are shown in Figs. 2(a)–(d). For all Ra these are nearly symmetric on either vertical side of the substrate, except very near the heat source. The relatively high R_s of 10 tends to efficiently conduct heat across the entire substrate, even though the heater is placed flush with its right side. As Ra increases, the extent of thermal stratification increases in the lower portion of the enclosure. Larger thermal gradients occur in the fluid next to the substrate and the enclosure top and sides.

Figures 2(a)–(d) also show changes in the streamline patterns with the expected increase in flow vigor with Ra. Two cells are formed within the enclosure, with the right cell being somewhat larger and stronger, due to the direct heater–fluid interaction. As Ra is increased, the centers of the cells move up and toward one another. Also, the fluid velocities in the lower right portion of the enclosure decrease.

The percentage heat loss rates through the component faces are shown in Fig. 3(a) for various Ra. As Ra is increased, the heat lost directly to the fluid, i.e. from the front face, is increased due to more vigorous convection. This increase takes place at the expense of the other three faces. As shown in Fig. 3(b), with increasing Ra, the heat lost from the top and bottom of the enclosure decreases and the heat lost to the sides of the enclosure increases. The heat loss through the enclosure bottom is below 5% for all Ra shown, decreasing with an increase in Ra due to increased thermal stratification near the bottom. There is a greater percentage of heat loss through the left wall than the right even though the right wall faces the component and the flow is stronger on the right. This is because the left wall, which acts as a heat sink, is closer to the substrate and heater than the right wall. It is interesting to note that the top wall dissipates almost half of the power generated by the component in the range of Ra examined.

The non-dimensional surface heat flux at the right solid–liquid boundary along the substrate and the corresponding surface temperatures were calculated as follows:

$$q = \frac{(T_s - T_f)}{\left(\frac{\delta Y_s}{\kappa_s} + \frac{\delta Y_f}{\kappa_f}\right)}, \quad T_{sur} = \frac{\left(\left(\frac{\delta Y_s}{\kappa_s}\right)T_f + \left(\frac{\delta Y_f}{\kappa_f}\right)T_s\right)}{\left(\frac{\delta Y_s}{\kappa_s} + \frac{\delta Y_f}{\kappa_f}\right)}. \tag{7a,b}$$

In equation (7), T_s and T_f are the respective temperatures at the solid and fluid nodes closest to the solid–fluid interface and δY_s and δY_f their corresponding normal distances from the interface. Along the component surface κ_s is replaced by κ_c. For the horizontal surfaces, the δY are replaced by δX. Heat fluxes are not defined at the corners. Similar relations can be written for the component–substrate interface. Two counter-clockwise contour distance coordinates are defined to display the resulting distributions in Figs. 4 and 5. $S1$ is the non-dimensional distance along the component surface with $S1 = 0$ at its lower right corner. $S2$ is defined along the substrate surface, starting at its lower right corner. Indeed the front face of the component is included in both $S1$ and $S2$.

Figure 4(a) shows the non-dimensional component surface heat flux distributions for various Ra. Generally similar trends are observed at each Ra. The component front face which is in direct contact with the liquid, has the lowest heat flux. The bottom face of the component has generally the greatest heat flux, with the maximum occurring near the bottom right corner. The top face has the second highest heat flux and the back face has a slightly lower heat flux. As seen later, at lower R_s these trends are modified. Figure 4(b) shows that the non-dimensional component surface temperatures also follow similar trends for all Ra. Surface temperatures are fairly uniform around the component with the highest temperature near the top on the front face. The high R_s and R_c values ensure reduced conductive resistance within the heater and the substrate.

The heat flux variations along the substrate are seen in Fig. 5(a). Only minor differences in trend are observed for the various Ra. The heat flux goes through a minimum at $S2 \approx 0.5$. This occurs due to the relatively weak flow below the source in conjunction with a decreasing temperature gradient due to a thickening thermal region adjacent to the substrate, seen in Figs. 2(a) and (b). For $S2 > 0.5$ the flux rapidly reaches its maximum value at $S2 \approx 2$, near the base of the component. The heat flux then decreases going up the component. Above the component, beyond $S2 = 3$, it decreases even more rapidly due to the increasing thermal layer thickness, going through a minimum at $S2 \approx 4.5$ prior to reaching the top right corner. Beyond the top right corner the heat flux decreases sharply again going over the top substrate face and comes to the minimum heat flux on the substrate at the midpoint of the top face at $S2 = 5.5$. Reviewing the temperature contours in Figs. 2(a)–(d), this is where the fluid temperature is the hottest next to the substrate.

The heat flux on the top face is nearly symmetric. Proceeding down the substrate left face, the heat flux goes through a small drop but quickly increases near the back of the component. It reaches a local maximum at the back of the base of the component at $S2 \approx 9$ and then decreases to a local minimum at $S2 = 10.25$. It then increases slightly to a local maximum near the bottom left corner at $S2 = 11$. The heat flux on the bottom face shows the same type of variation as the top. However the values are higher due to the colder fluid in the vicinity of the bottom face.

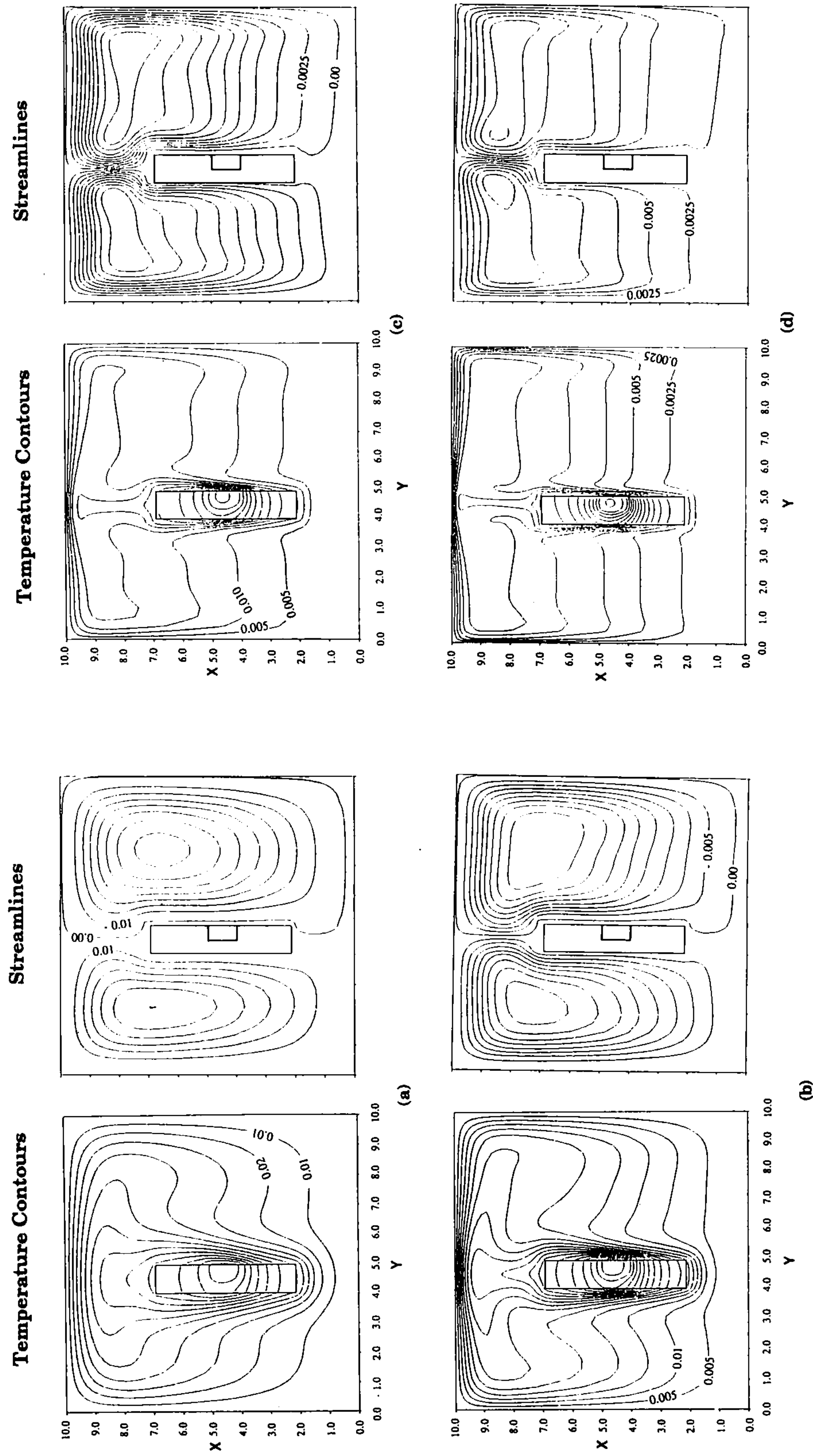

FIG. 2. Temperature contours and streamlines for: (a) $Ra = 10^3$; (b) $Ra = 10^4$; (c) $Ra = 10^5$; (d) $Ra = 10^6$. Other parameters are at their baseline values. Location of heat source is shown with the streamline contours.

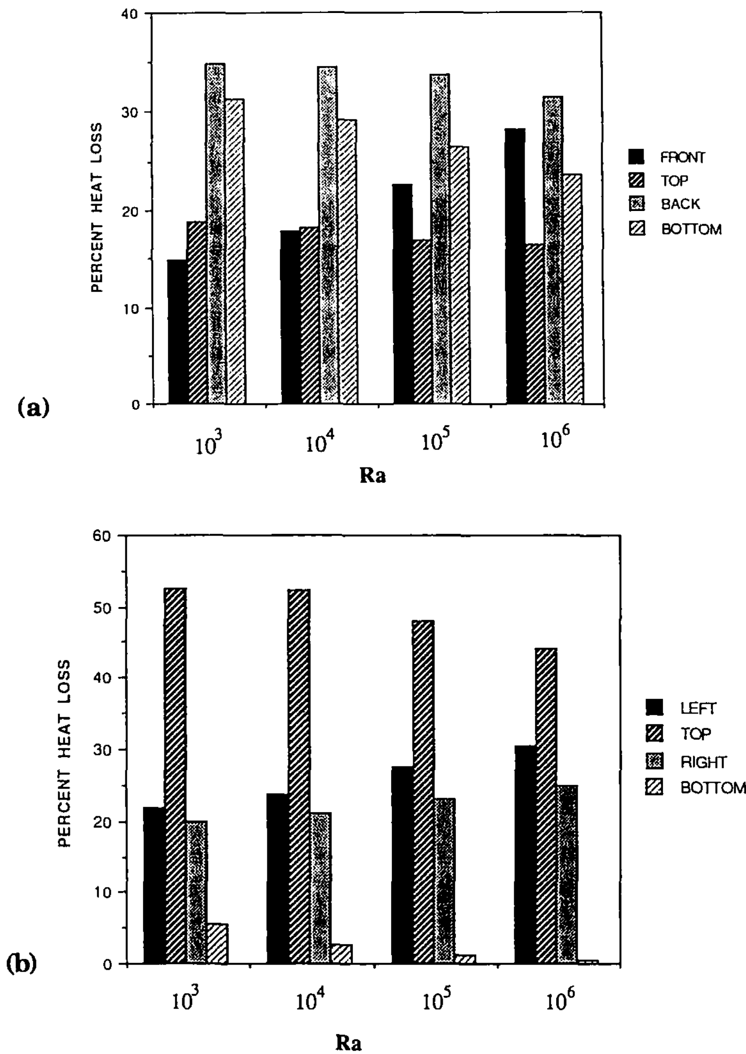

FIG. 3. Percentage heat loss rates at various Ra from: (a) the component faces; (b) the four enclosure walls.

Non-dimensional substrate surface temperatures T_{sur} for various Ra are shown in Fig. 5(b). The lowest temperatures are at the bottom of the substrate and the highest at the top of the component. Local maxima are evident at the back of the substrate due to direct conduction from the heater. The higher the Ra, the greater the vigor of the buoyancy induced flow and the resulting heat transfer from the component, leading to lower non-dimensional temperatures.

B. *Effect of Pr*

Computations were carried out for $Pr = 7$, 25 and 100. These cover the range of liquids from water to the dielectric Fluorinerts used in liquid immersion cooling. It was found [20] that with other parameters remaining constant, Pr had a negligible effect on the computed non-dimensional temperature contours and streamlines. This indicates that the results of experimental studies in water with $Pr = 7$ would apply to the dielectric liquids as well, for the same value of Ra and other parameters.

C. *Effect of substrate conductivity ratio* R_s

The streamlines and temperature contours for various R_s for $Ra = 10^5$ are shown in Figs. 6(a)–(d). For $0.1 \leqslant R_s \leqslant 1$ a stronger flow is generated on the heater side with a relatively weak cell on the left side of the enclosure. Temperature contours show a large gradient just outside the component for $R_s = 0.1$ and a hot spot at the top left corner. For $R_s = 1$ the maximum temperature location moves towards the center of the component and as R_s increases further, it moves towards the fluid. For R_s above 10 the two cells on the opposite sides of the substrate are of about the same strength. Temperature contours and streamlines show almost no dependence on R_s for $R_s > 10$.

The percent heat loss through the component faces

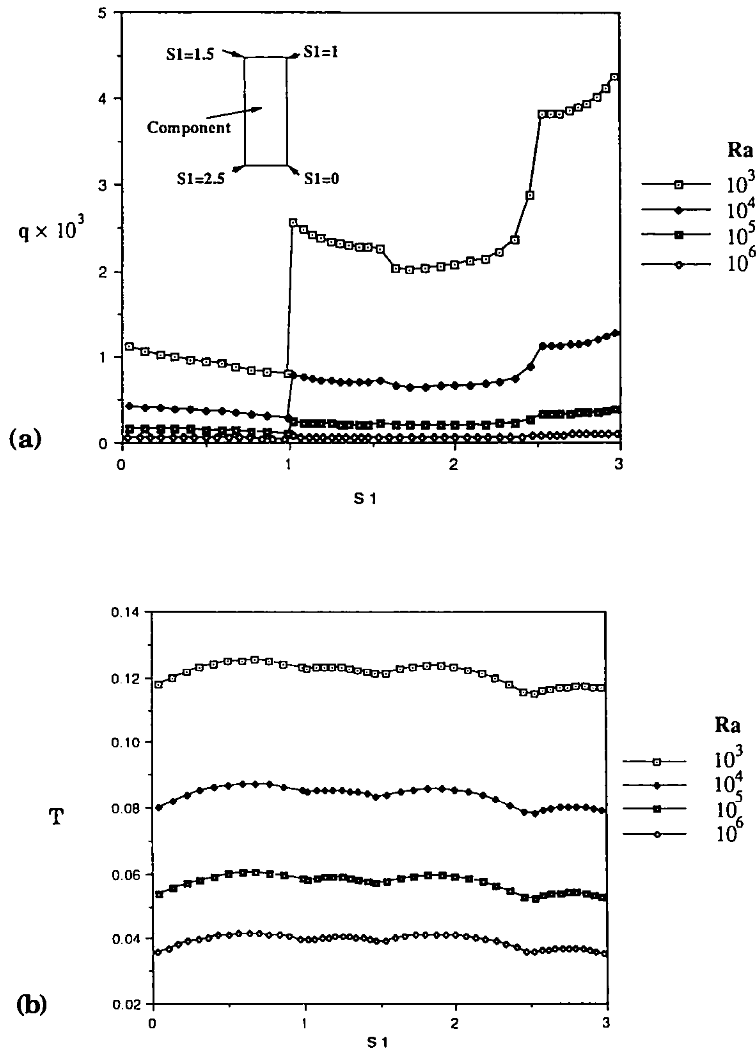

FIG. 4. Distributions of (a) surface heat flux and (b) surface temperature along the component for various Ra.

for various R_s are seen in Fig. 7(a) for $Ra = 10^5$. There is a large drop in the percent heat loss to the fluid from the front face when R_s is increased from 0.1 to 10, after which it shows only a slight decrease. As R_s increases, it is easier for the heat to flow through faces other than the front. The substrate acts like a fin, increasing the surface area for heat loss. The back face percent heat loss increases throughout the range of R_s increase. The bottom and top face percent heat losses increase when R_s is increased from 0.1 to 10 and then remain fairly constant.

The percent heat losses through the enclosure walls for various R_s are shown in Fig. 7(b). As R_s increases from 0.1 to 1 the bottom wall loss decreases slightly as the left recirculating region brings higher temperatures closer to the bottom wall. A gradual increase over the remaining range of R_s occurs due to the increased heat conduction through the bottom portion of the substrate into the vicinity of the bottom enclosure wall. The percentage heat loss through the top face displays a minimum for $10 \leq R_s \leqslant 50$. An initial decrease in this fraction in the range $0.1 \leqslant R_s \leqslant 10$ results due to the increasing flow vigor of the cells on either sides of the substrate, which facilitates the transport of warm liquid to the vicinity of the sidewalls. For $R_s > 10$, a strong buoyant plume is shed above the substrate which impinges on the top boundary, causing an increase in the heat removal rate from it. The heat loss changes at other boundaries are a result of these flow changes.

The component surface heat flux distributions are seen in Fig. 8(a) for various R_s. For $R_s = 0.1$ and 1 the highest heat flux is along the component–liquid interface, for $S1 = 0$. This flux decreases downstream starting from $S1 = 0$. At higher R_s this trend is modified. The generated energy is now conducted more

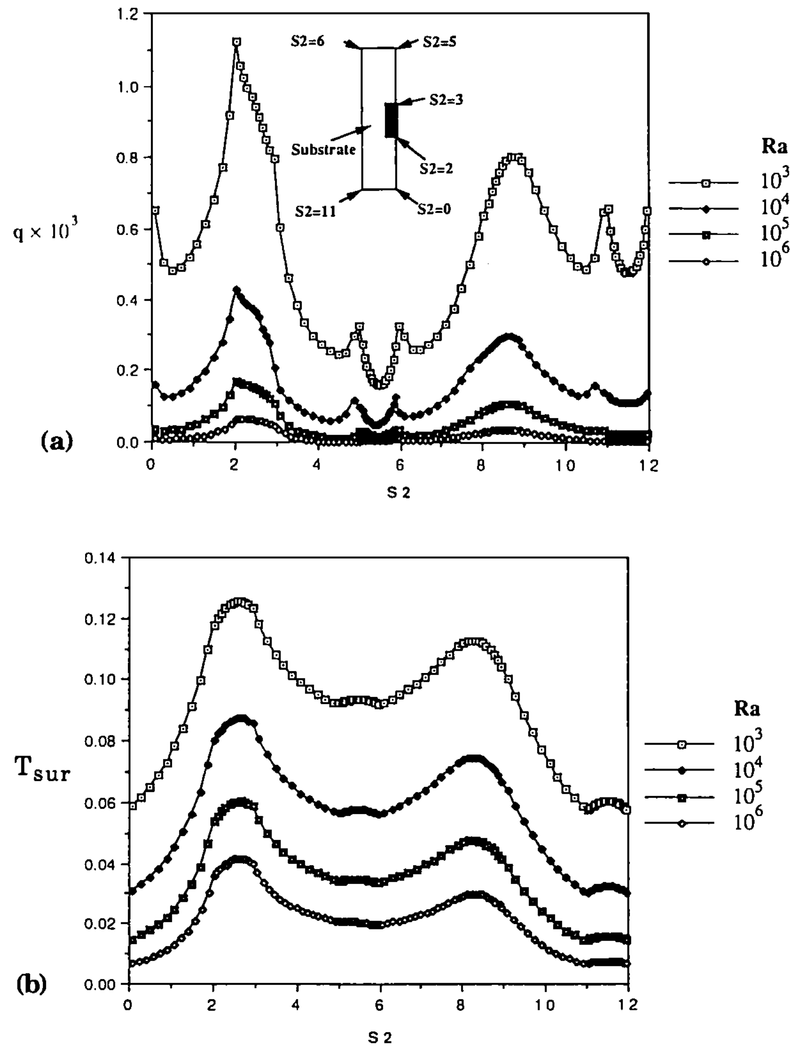

FIG. 5. Distributions of (a) surface heat flux and (b) surface temperature along the substrate for various Ra.

efficiently along the substrate, resulting in local maxima near the centers of each of the three component faces in contact with the substrate. The largest of these occurs along the bottom face, due to the ability of the lower substrate extension to transport heat to the relatively cold stratified liquid. The heat flux distributions remain almost unchanged above $R_s = 50$.

The component–fluid and substrate–fluid interface temperatures for various R_s seen in Fig. 8(b) are fairly uniform for $R_s \geqslant 10$. For $R_s < 10$ the temperatures are higher over the component surface, with the maximum occurring at the top of the component, at $S2 = 3$. Computations of maximum temperature revealed little benefit in increasing R_s beyond 10.

The present computations of component front face temperatures in the limit of $R_s \ll 1$ and $R_c \gg 1$ can be compared to the uniform heat flux flat plate correlation of Fujii and Fujii *et al.* [21]. In the present variables, the local surface temperature variation along the component for $0 \leqslant S1 \leqslant 1$ from ref. [21] is given as

$$T = (S1/Ra)^{1/5}/F(Pr), \quad \text{where} \quad F(Pr) = [Pr/(4+9Pr^{1/2}+10Pr)]^{1/5}. \quad (8)$$

For $Pr = 25$ and $Ra = 10^5$ the computed values of T at $S1 = 0.5$ and 1.0 from equation (8) are 0.143 and 0.164, respectively. The corresponding values from the present model for $R_s = 0.1$ are 0.131 and 0.134. These smaller values indicate small but non-zero substrate conduction which occurs from the three substrate exposed component faces. Also, Fig. 8(a) clearly shows that the uniform heat flux boundary condition used in equation (8) is not an accurate assumption for the present computations.

The heat flux distributions along the substrate for $R_s \geqslant 10$ displayed larger uniformity due to the efficient

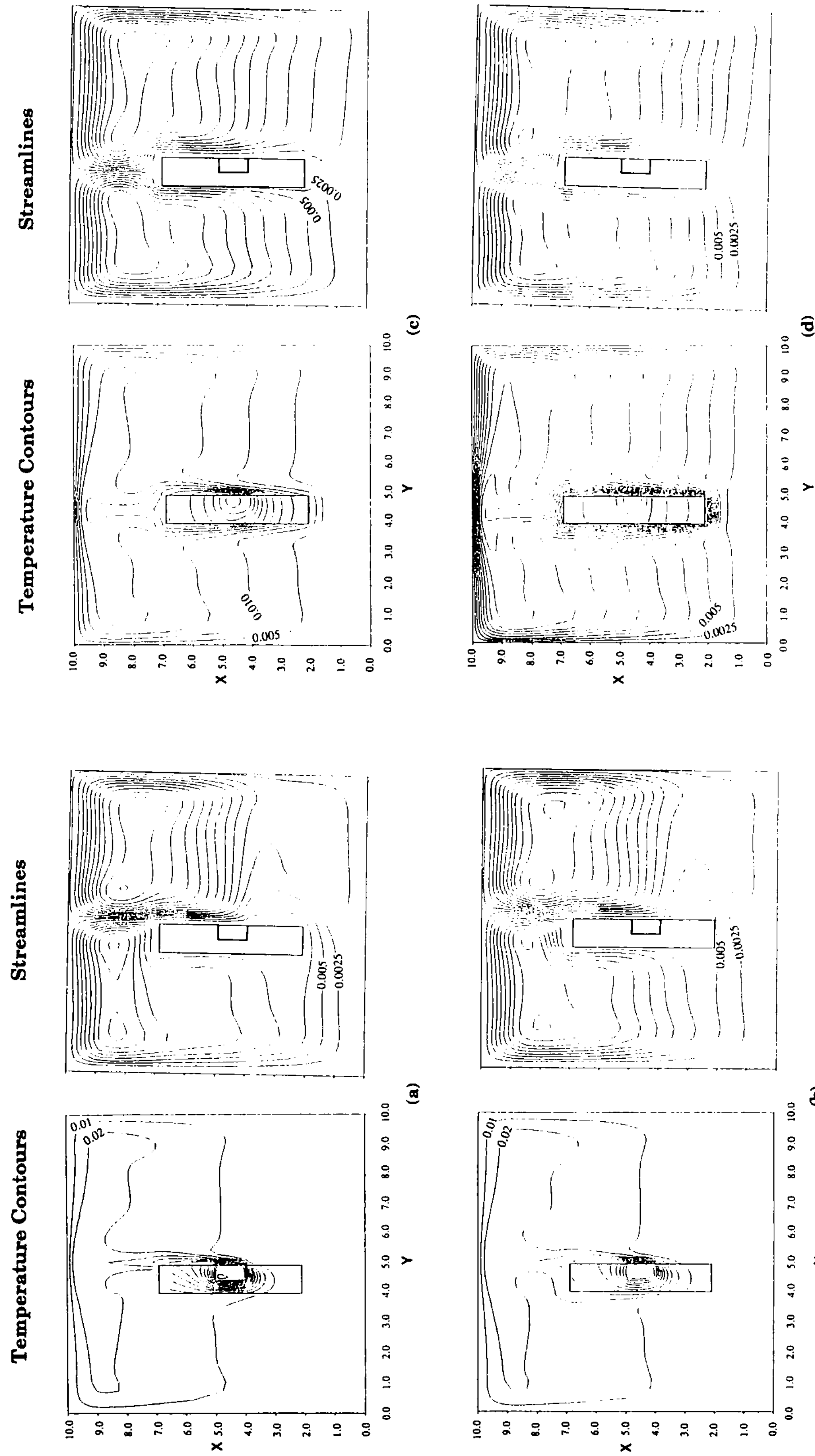

FIG. 6. Effect of substrate thermal conductivity variation. Temperature contours and streamlines are for: (a) $R_s = 0.1$; (b) $R_s = 1$; (c) $R_s = 10$; (d) $R_s = 100$. Other parameters are at their baseline values.

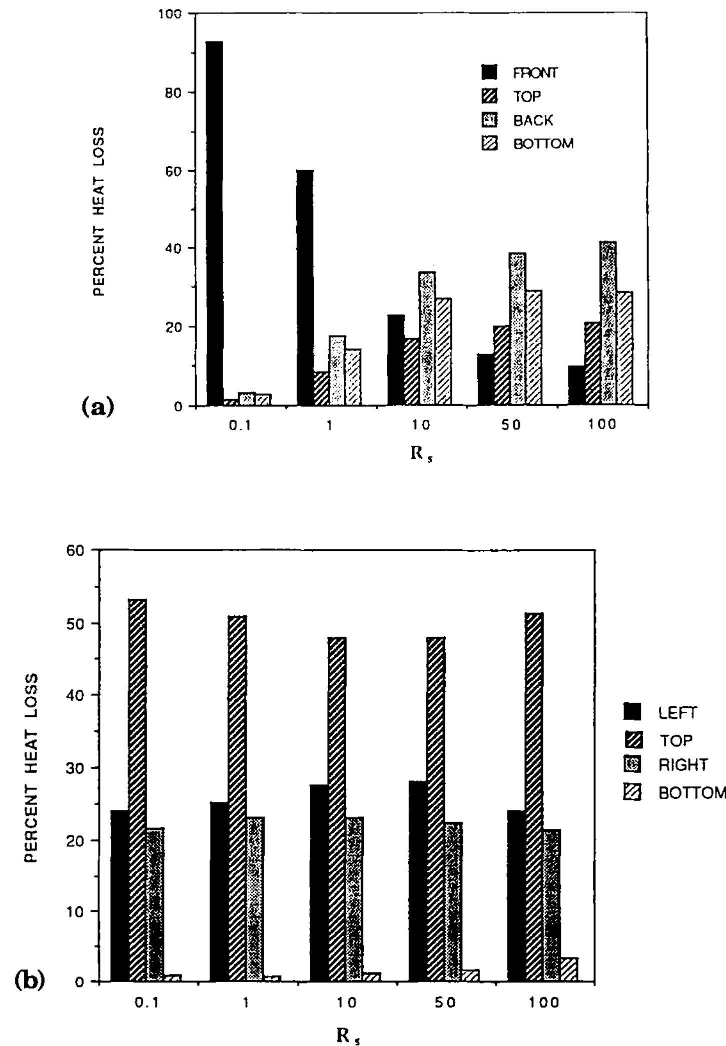

FIG. 7. Percentage heat loss rates at various R_s from (a) the component faces and (b) the four enclosure walls.

heat spreading. For lower R_s the largest heat flux was along the front face of the component, $S2 = 2$–3, with its maximum value near the bottom of the component at $S2 = 2$. For $R_s \leqslant 1$ small negative heat flux values were found [20] for $S2 = 4$–5, indicating heat transfer to the substrate by the warm fluid above the component.

D. *Effect of component conductivity ratio* R_c

The effects of R_c on the temperature contours are shown in Figs. 9(a)–(c). For $R_c = 1$ (a), there is a steep thermal gradient within the component with the maximum temperature near its center. For $R_c = 25$, (b), the hot spot has moved towards the fluid exposed face and the component is almost at a uniform temperature. For $R_c = 50$ and above, the temperature contours look identical. These are seen in Fig. 9(c) for $R_c = 100$. There was a negligible change in the streamlines for the entire range of R_c studied. The flow patterns resembled those in Fig. 2(c) for all cases and are therefore not presented.

The percent heat loss rates through the component faces are shown in Fig. 10. With R_c increasing from 1 to 25, there is a large decrease in the percent heat loss from the front face and a slight decrease from the back. A large increase in the percent heat loss from the bottom and a slight increase in the top face make up for the decrease at the front and back. The relatively high R_s ensures efficient conduction along the substrate extensions above and below the source. As R_c increases beyond 25 there is only a weak increase in the bottom percent heat loss at the expense of the front and the back losses. The bottom face uses the substrate below as a fin to conduct heat to the lower cooler region of the enclosure. The heat loss fractions through the enclosure walls changed insignificantly, which is expected due to almost no change in the fluid flow or the temperature distributions in the fluid over the entire range of R_c studied.

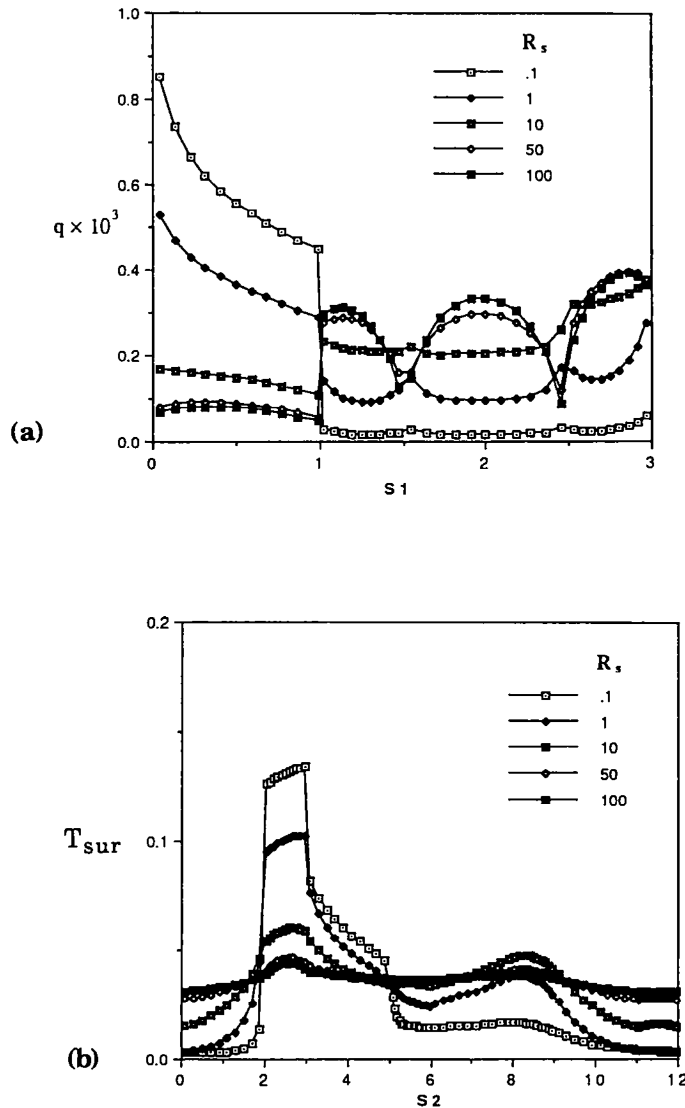

FIG. 8. Distributions of (a) component surface heat flux and (b) surface temperature along the substrate for various R_s.

The component surface heat flux, Fig. 11(a), shows a similar pattern for each face for $R_c = 1$. Each face has a local maximum near the center with the largest of these at the center of the back face at $S1 = 2$. The maxima along each face exist at the largest normal temperature gradient locations, typically arising at the mid-faces. For $25 \leqslant R_c \leqslant 100$, the component surface heat fluxes change relatively weakly, with the greatest flux going through the bottom face near the fluid–component boundary. The flux is greatest here due to the substrate extension below the component. In addition, the induced flow adjacent to the substrate below the bottom of the component augments heat transfer from the front substrate surface below the heat source.

The component surface temperatures for $R_c = 1$, seen in Fig. 11(b), also display local maxima along each face. The largest of these occurs on the fluid exposed face at $S1 \approx 0.7$. Since the fluid thermal conductivity is the same as that of the source for this condition, the direct heat transfer from the component to the fluid is rather poor. For $25 \leqslant R_c \leqslant 100$ the temperature over the various surfaces is more uniform. The maximum temperature computations showed little advantage in increasing R_c above 25.

COMPARISON WITH EXISTING MEASUREMENTS

Temperature predictions from the present model were compared with existing measurements for a sub-

FIG. 9. Effect of component thermal conductivity variation. Temperature contours are for: (a) $R_c = 1$; (b) $R_c = 25$; (c) $R_c = 100$. Other parameters are at their baseline values.

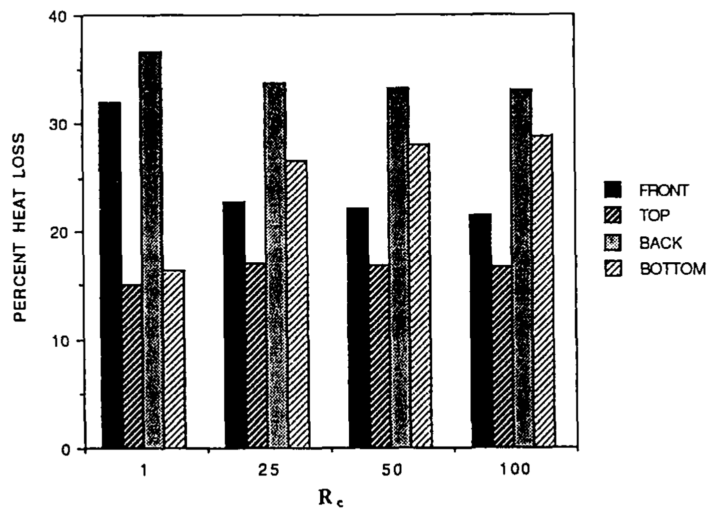

FIG. 10. Percentage heat loss rates at various R_c from the component faces.

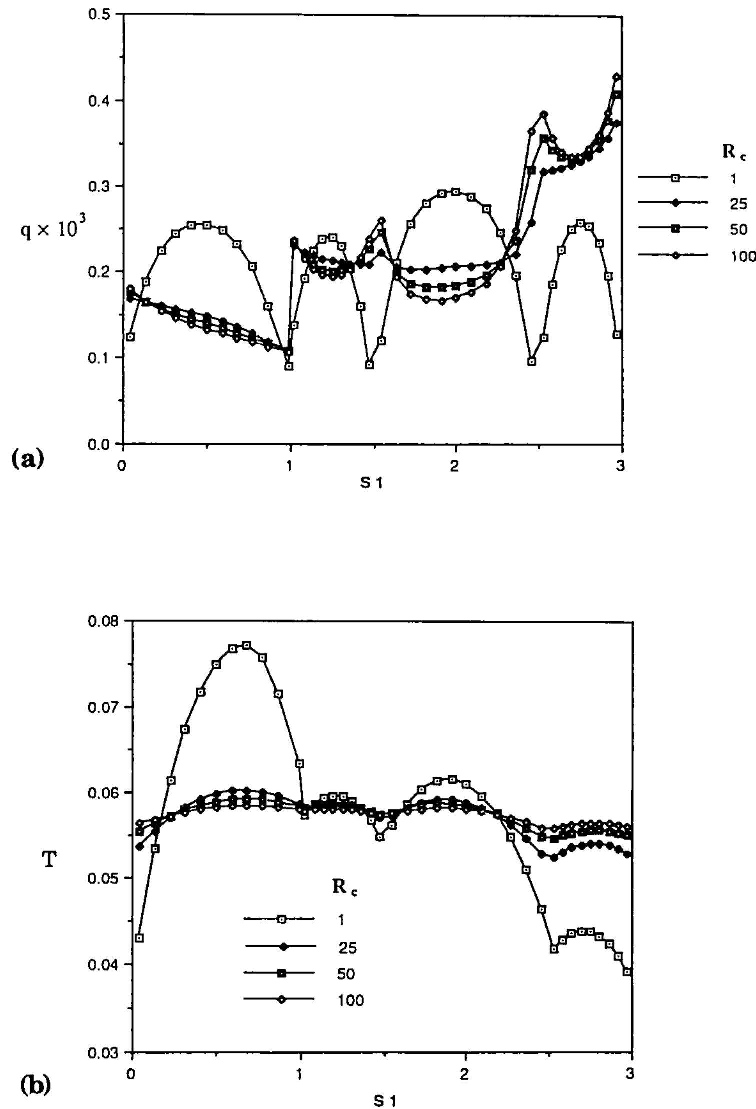

FIG. 11. Distributions of (a) surface heat flux and (b) surface temperature along the component for various R_c.

strate mounted discrete heat source in water [13]. The experiments investigated the transport from a column of heaters flush mounted on a vertical plexiglass substrate both without and with a parallel shrouding wall. Temperature responses were measured first with all elements in the column uniformly powered. The effective vertical spacing between heaters was then increased by having only some components powered. Temperatures at the center of the lowest heater in the column were almost unaffected by these changes in downstream heating. Also, flow visualizations in ref. [13] showed that with no shroud, the flow was primarily two-dimensional near the center of the bottom heater. Temperature measurements at the center of the bottom heater in the absence of shroud were therefore used for comparisons with the computations.

A schematic of the model geometry with the thermocouple location identified is provided in Fig. 12(a). The thermofoil heater consisted of an Inconel ribbon mounted over a Kapton backing. In the computations, the heater element was modeled as a two-layer composite with the entire heat generation taking place in the Inconel. While the Kapton backing for the actual heater was 7.8 mm high and 23.9 mm wide, the region which contained the Inconel was only 6.2 mm high and 22.0 mm wide. The energy generation term in the model was therefore prescribed to be non-zero only within this region.

The experiments described above were carried out in a large water tank. In the computations, a rectangular enclosure was prescribed around the heater with its walls at the ambient temperature. The enclosure walls were placed sufficiently far from the heater so that moving them further away had only a neg-

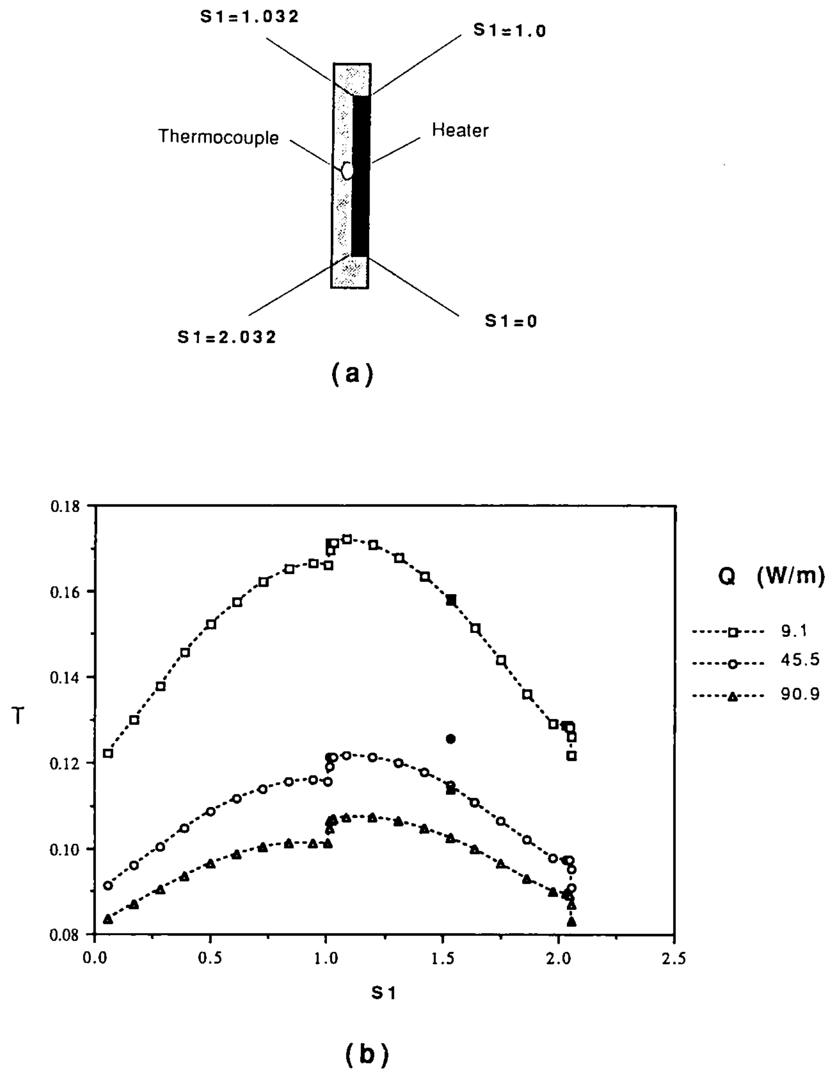

FIG. 12. Comparison of predicted component temperatures with existing data. The idealized bottom component from the experiments in ref. [13] is seen in (a). In (b) the computed surface temperatures along the component are shown as open symbols joined with dashed lines. The measured values at the back of the component for the corresponding power levels are shown as filled symbols.

ligible effect on the heater temperatures. The geometric parameters used in the computations were: $H/h = 10$, $d/h = 2$, $L_t/h = 2$, $S_t/h = 3$, $S_b/h = 2$, $d_t/h = 1.5$ and $w/h = 0.032$. The thermophysical properties resulted in $R_s = 0.231$, $R_c = 21.47$ and $Pr = 6.67$.

The resulting comparisons are seen in Fig. 12(b). The agreement between the model and measurements at the center of the rear heater surface, $S1 = 1.53$, is within 1% at the lowest component power input of 0.2 W. The measured component temperatures at higher power levels had larger deviations. At 1.0 and 2.0 W power inputs the percent differences are approximately 9 and 10%, respectively.

These differences are the net result of several factors. The Inconel region of the heater was taken as a uniform heat source in the model but in reality was a ribbon distributed on the Kapton sheet. At higher power levels this could cause hotter areas near the ribbon, an effect not accounted for in the computations. For these power levels, the spanwise entrainment of warmer fluid from the lateral edges of the heater towards the central plane may necessitate a three-dimensional transport model. Also, the properties for the water used in the model were taken at a film temperature assumed to be the average temperature of the heater and the ambient water. Variable properties may have to be assumed at the high component powers.

CONCLUSIONS

The following conclusions can be drawn based on the present study:

(1) Constant surface heat flux or temperature boundary conditions are often inappropriate for substrate mounted discrete heat generating elements.

(2) Changes in Pr between 7 and 100 had an insignificant effect on the non-dimensional temperatures. This allows the use of experimental data for liquids such as water for studying liquid immersion cooling, as long as the values of Ra and other non-dimensional parameters can be duplicated.

(3) Increasing R_s provides substantial cooling enhancement when R_s is less than 10 but only marginal improvements for larger values, for all other fixed parameters.

(4) An increase in R_c provides lower and more uniform component temperatures primarily for R_c less than 25, for all other parameters maintained the same.

Acknowledgements—This study was supported by a grant from the Naval Surface Warfare Center, Crane, Indiana, under the SHARP program.

REFERENCES

1. A. Bar-Cohen, Thermal management of electronic components with dielectric liquids, *Proc. ASME/JSME Thermal Engng Joint Conf.*, Vol. 2, pp. xv–xxxix (1991).
2. A. E. Bergles and A. Bar-Cohen, Direct liquid cooling of microelectronic components. In *Advances in Thermal Modeling of Electronic Components and Systems* (Edited by A. Bar-Cohen and A. D. Kraus), Vol. 2, pp. 233–342. ASME Press (1990).
3. F. P. Incropera, Convection heat transfer in electronic equipment cooling, *ASME J. Heat Transfer* **110**, 1097 (1988).
4. Y. Jaluria, Natural convective cooling of electronic equipment. In *Natural Convection Fundamentals and Applications* (Edited by S. Kakac, W. Aung and R. Viskanta), pp. 961–986. Hemisphere, New York (1985).
5. Y. Jaluria, Interaction of natural convection wakes arising from thermal sources on a vertical surface, *ASME J. Heat Transfer* **107**, 883 (1985).
6. H. L. Chadwick, B. W. Webb and H. S. Heaton, Natural convection from two-dimensional discrete heat sources in a rectangular enclosure, *Int. J. Heat Mass Transfer* **34**, 1679 (1991).
7. S. Lee and M. M. Yovanovich, Conjugate heat transfer from a vertical plate with discrete heat sources under natural convection, ASME Paper No. 89-WA/EEP-9 (1989).
8. M. Afrid and A. Zebib, Natural convection air cooling of heated components mounted on a vertical wall, *Numer. Heat Transfer, Part A* **15**, 243 (1989).
9. K. A. Park and A. E. Bergles, Natural convection heat transfer characteristics of simulated microelectronic chips, *ASME J. Heat Transfer* **109**, 90 (1987).
10. M. D. Kelleher, R. H. Knock and K. T. Yang, Laminar natural convection in a rectangular enclosure due to a heated protrusion on a vertical wall—Part I: experimental investigation, *Proc. Second ASME/JSME Thermal Engng Joint Conf.*, Honolulu, p. 169 (1987).
11. M. Keyhani, V. Prasad and R. Cox, An experimental study of natural convection in a vertical cavity with discrete heat sources, *ASME J. Heat Transfer* **110**, 616 (1988).
12. Y. Joshi, M. D. Kelleher and T. J. Benedict, Natural convection immersion cooling of an array of simulated electronic components in an enclosure filled with dielectric fluid. In *Heat Transfer in Electronic and Micro-Electronic Equipment* (Edited by A. E. Bergles), p. 445. Hemisphere, New York (1990).
13. Y. Joshi and D. L. Knight, Natural convection from a column of flush heat sources in a vertical channel in water, *ASME J. Electron. Packaging* **112**, 367 (1990).
14. J. J. Lee, K. V. Liu, K. T. Yang and M. D. Kelleher, Laminar natural convection in a rectangular enclosure due to a heated protrusion on one vertical wall—Part II: numerical simulation, *Proc. Second ASME/JSME Thermal Engng Joint Conf.*, Honolulu, p. 179 (1987).
15. K. V. Liu, K. T. Yang and M. D. Kelleher, Three dimensional natural convection cooling of an array of heated protrusions in an enclosure filled with a dielectric fluid, *Proc. Int. Symp. on Cooling Technology for Electronic Equipment*, Honolulu, p. 179 (1987).
16. S. B. Sathe and Y. Joshi, Natural convection from a heat generating substrate-mounted protrusion in a liquid filled two-dimensional enclosure, *Int. J. Heat Mass Transfer* **34**, 2149 (1991).
17. S. V. Patankar, *Numerical Heat Transfer and Fluid Flow*. Hemisphere/McGraw-Hill, New York (1980).
18. G. D. Raithby and H. H. Wong, Heat transfer by natural convection across vertical air layers, *Numer. Heat Transfer* **4**, 447 (1981).
19. Product Manual, Fluorinert Electronic Liquids, 3M Corporation, St. Paul, Minnesota (1985).
20. L. O. Haukenes, A computational and experimental study of flush heat sources in liquids, M. E. Thesis, Naval Postgraduate School, Monterey (1990).
21. T. Fujii and M. Fujii, The dependence of local Nusselt number on Prandtl number in the case of free convection along a vertical surface with uniform heat flux, *Int. J. Heat Mass Transfer* **19**, 121 (1976).